Springer

KSME

Journal of Mechanical Science and Technology 33 (7) (2019) 3555~3562
www.springerlink.com/content/1738-494x(Print)/1976-3824(Online)
DOI 10.1007/s12206-019-0649-7

Numerical study on cooling performance of hybrid micro-channel/micro-jet-impingement heat sink †

Seong Hoon Kim, Hong-Cheol Shin and Sung-Min Kim*

School of Mechanical Engineering, Sungkyunkwan University, 300 Cheoncheon-dong, Suwon 16419, Korea

(Manuscript Received November 13, 2018; Revised February 17, 2019; Accepted April 22, 2019)

Abstract

This study explores the cooling performance associated with single-phase hybrid micro-channel/micro-jet-impingement cooling method. A parametric study on the geometrical and operating parameters of hybrid cooling is numerically investigated. Appreciable temperature drop on the bottom surface of the micro-channel is achieved as a result of the strong impingement effects caused by reduced diameter of jet inlets, while the temperature on the bottom surface of the micro-channel increases with increasing the number of jet inlets due to weak impingement effects. The results also show that mean convective heat transfer coefficient of bottom wall can be achieved up to 11152 W/m^{2}K using five jet inlets with diameter of 0.19 mm each.

Keywords: High-heat-flux; Micro-channel heat sink; Micro-jet-impingement cooling; Thermal management

1. Introduction

Removal of high-heat-flux dissipated by electronic components is necessitated by micro-miniaturization of electronic and power devices, thus increased circuit density. Therefore, innovative thermal designs are becoming more important in the development of such devices. Not only eliminating high-heat-flux from device but also maintaining low device temperature is a primary concern in thermal design of high performance devices, because the low temperature with which the electronic devices operate could improve the electrical performances [1, 2]. To meet these cooling requirements, the micro-channel heat sinks as well as the micro-jet-impingement have been developed as a cooling solution of today's high-end devices [3].

The merits of micro-channel heat sinks are the ability to produce high heat transfer coefficients and to reduce coolant inventory [4-6]. However, disadvantages of micro-channel heat sink are its large pressure drop and temperature rise [6]. Jet impingement heat transfer has been investigated numerically [7-10] and experimentally [11-13]. These studies show single jet impingement heat transfer achieves high heat transfer coefficient in the impingement zone, while sudden increase in surface temperature away from impingement zone can occur due to the abrupt decrease of heat transfer coefficient. To solve these problems, multiple jets are used to dampen such a large variation of temperature by distributing the impingement zones along the impingement surface [14,15]. However, also shown in using multiple jets is the disadvantage, which associates with the flow blockage due to the liquid interference between neighboring jets subsequent its impingement onto the surface [16].

Among thermal design endeavors for capitalizing upon the advantages of both micro-channel heat sinks and micro-jet impingement, Sung and Mudawar [17] proposed hybrid micro-channel/micro-jet-impingement cooling method. They found that using this method the temperature can be uniform across the heated surface while dissipating large amounts of heat. Sung and Mudawar [18] showed that both the surface temperature and temperature gradient along the channel decreased with decreasing channel width, and that the surface temperature decreased with decreasing channel height for high jet velocity, while opposite trend was shown for low jet velocity. Sung and Mudawar [19] examined the cooling performance of three micro-jet patterns including decreasing-jet-size, equal-jet-size, and increasing-jet-size. They found that the decreasing-jet-size pattern provided the highest heat transfer coefficient among three patterns.

In this study, the effects of the number of jets and the size of jet diameter on the cooling performance of hybrid micro-channel/micro-jet-impingement heat sink are numerically investigated through examination of hydrodynamic and thermal characteristics of heat sink.

*Corresponding author. Tel.: +82 31 290 7433, Fax.: +82 31 290 5889
E-mail address: smkim@skku.edu
† Recommended by Associate Editor Seong Hyuk Lee

Table 1. Design parameter used in the present study.

N_{jet}	5, 7, 10
D_{jet} [mm]	0.19, 0.39, 0.59
q''_{bot} [W/cm^2]	10, 50, 100, 150
$\dot{m}$ [g/s]	2, 5, 8

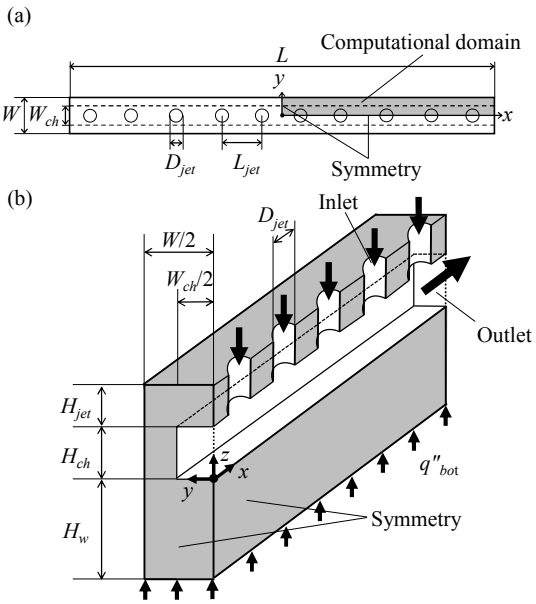

Fig. 1. Schematic of computational domain of hybrid micro-channel/micro-jet-impingement heat sink showing a single row of micro-channel: (a) Top view; (b) isometric view.

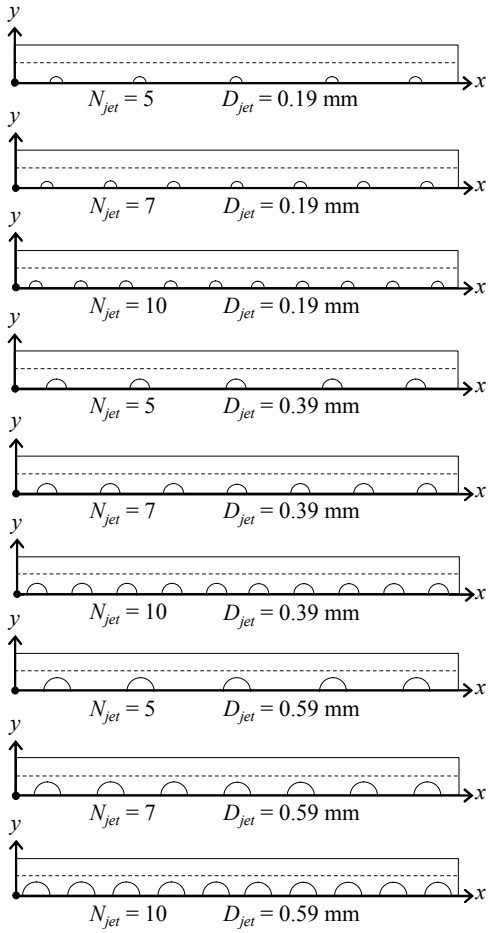

Fig. 2. Different micro-jet geometries.

2. Numerical method

Fig. 1(a) shows schematics of single row of micro-jets and single micro-channel using HFE 7100 as working fluid. As shown in Fig. 1(b), the computational domain includes one quarter of the flow channel and the surrounding copper due to symmetry planes at $x = 0$ and $y = 0$. The velocity inlet and pressure outlet boundary conditions are applied to the inlets of micro-jets and outlet of the micro-channel, respectively. Uniform heat flux is applied to the bottom wall. Three surfaces of solid at $x = L/2$, $y = W/2$, and $z = H_{ch} + H_{jet}$, respectively, are assumed adiabatic. Different micro-jet geometries, shown in Fig. 2, are used to investigate the parametric effects associated with geometrical parameters. For grid independence test, three grid systems, with 595625, 756228 and 963238 cells, are used. 756228 cells are then selected since the discrepancy between 756228 and 963238 cells for the mean temperature of micro-channel's bottom wall is less than 1 %. The realizable k-ε turbulent model [20] is used for solving Reynolds stress tensor in Reynolds averaged Navier-Stokes equation. Semi-implicit method for pressure-linked equations-consistent (SIMPLEC) algorithm [21] is used to solve the discretized governing differential equations by using ANSYS FLUENT [22]. Table 1 summarizes the geometrical and operating parameters used in this study. The ranges of jet Reynolds number, Re_j $(= 4\dot{m} / \pi\mu D_{jet} N_{jet})$, and channel Reynolds number, Re_{ch} $(= 4\dot{m} / \mu(W_{ch} + H_{ch}))$, used in the present study are 480–11913 and 1111–4444, respectively.

The flow and heat transfer characteristics of the heat sink were examined numerically by solving the conjugate heat transfer problem. For the fluid region, the governing equation for steady, incompressible and turbulent flow can be expressed, respectively, as

Mass conservation:

$$\frac{\partial u_i}{\partial x_i} = 0 . \tag{1}$$

Momentum conservation:

$$\rho_f u_j \frac{\partial u_i}{\partial x_j} = -\frac{\partial P}{\partial x_i} + \mu \frac{\partial}{\partial x_j}\left(\frac{\partial u_i}{\partial x_j}\right) - \rho_f \frac{\partial}{\partial x_j}\left(\overline{u_i' u_j'}\right). \tag{2}$$

Energy conservation:

$$\rho_f c_{p,f} u_j \frac{\partial T}{\partial x_j} = \frac{\partial}{\partial x_j}\left[\left(k_f + \frac{c_{p,f}\mu_t}{Pr_t}\right)\frac{\partial T}{\partial x_j}\right]. \tag{3}$$

By using Boussinesq hypothesis, Reynolds stress tensor

$(-\rho_f \overline{u_i' u_j'})$ can be expressed as

$$-\rho_f \overline{u_i' u_j'} = \mu_t \left(\frac{\partial u_i}{\partial x_j} + \frac{\partial u_j}{\partial x_i} \right) - \frac{2}{3} \rho_f k \delta_{ij} . \quad (4)$$

Realizable k-ε turbulent equations are used to calculate eddy viscosity, μ_t. Turbulent kinetic energy equation and turbulent dissipation rate equation can be expressed as

Turbulent kinetic energy equation:

$$\rho_f \frac{\partial}{\partial x_j}\left(k u_j\right) = \frac{\partial}{\partial x_j}\left[\left(\mu + \frac{\mu_t}{\sigma_k} \right) \frac{\partial k}{\partial x_j} \right] + G_k - \rho_f \varepsilon . \quad (5)$$

Turbulent dissipation rate equation:

$$\rho_f \frac{\partial}{\partial x_j}\left(\varepsilon u_j\right) = \frac{\partial}{\partial x_j}\left[\left(\mu + \frac{\mu_t}{\sigma_\varepsilon} \right) \frac{\partial \varepsilon}{\partial x_j} \right] + \rho_f C_1 S \varepsilon - \rho_f C_2 \frac{\varepsilon^2}{k + \sqrt{\nu \varepsilon}} . \quad (6)$$

For the solid regions, a constant heat flux is applied to the bottom of copper block.

$$-k_s \frac{\partial T}{\partial z} = q''_{bot} . \quad (7)$$

3. Results and discussion

To assess the validity of the numerical model used in this study, computed temperature distributions along $0 \le x \le L/2$ at $y = 0$ and $z = -2.54$ mm are compared with previous experimental data by Sung and Mudawar [18] for $N_{jet} = 7$ and $D_{jet} = 0.39$ mm with two different sets of boundary conditions. Fig. 3 shows excellent agreement between computed temperature distributions and experimental data, and verifies the predictive capability of present numerical model. Therefore, all of the subsequent numerical simulations with different geometrical and operating parameters are based on the present numerical model.

Fig. 4 shows streamline plots along the x-z plane at $y = 0$ mm, and convection heat transfer coefficient distributions of the micro-channel's bottom wall for different N_{jet} and D_{jet} at $q''_{bot} = 50$ W/cm^2 with $\dot{m} = 5$ g/s. The local heat transfer coefficient is defined by dividing the local heat flux at the micro-channel's bottom wall by the difference between the local temperature at the micro-channel's bottom wall and HFE 7100 temperature at the jet inlet. In Fig. 4(a), for $N_{jet} = 5$ with $D_{jet} = 0.19$ mm, the HFE 7100 from all jets reaches the micro-channel's bottom wall and forms the impingement zones due to the strong impingement effects. As a result, high heat transfer coefficient is achieved over the entire micro-channel's

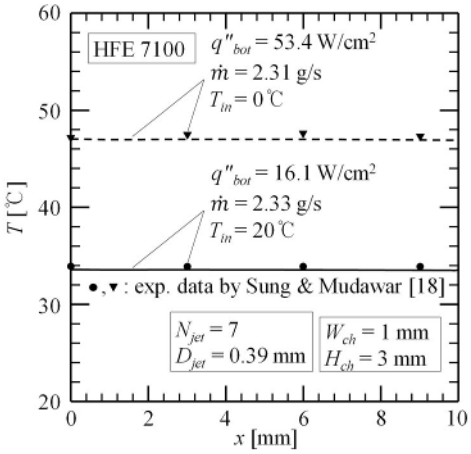

Fig. 3. Comparison of present computed temperature distributions with previous experimental data by Sung and Mudawar [18] along $0 \le x \le L/2$ at $y = 0$ and $z = -2.54$ mm.

bottom wall. Especially for $N_{jet} = 10$ with $D_{jet} = 0.19$ mm (see Fig. 4(b)) and $N_{jet} = 5$ with $D_{jet} = 0.59$ mm (see Fig. 4(c)), sharp variation in heat transfer coefficient occurs in the impingement zone formed by the first jet. This is because the HFE 7100 from the first jet reaches the micro-channel's bottom wall and forms the impingement zone, while the HFE 7100 from the other downstream jets are difficult to reach the micro-channel's bottom wall and do not form the impingement zones since the jet's momentum from downstream jets appears to be not enough to penetrate the micro-channel flow accumulated gradually from the upstream jets. For $N_{jet} = 10$ with $D_{jet} = 0.59$ mm (see Fig. 4(d)), the HFE 7100 from the first jet reaches the micro-channel's bottom wall, and forms the impingement zone. The heat transfer coefficient, however, is very small over the entire micro-channel's bottom wall due to the low momentum of the jet.

The relationship between momentum of the HFE 7100 and thermal boundary layer is examined in Fig. 5. Shown in Fig. 5(a) is the temperature distribution in cross-section on the y-z plane at the first jet ($x = 1$ mm) for $N_{jet} = 5$ with $D_{jet} = 0.19$ mm where the jet impingement effect is dominant. Fig. 5(b) illustrates the temperature distributions in cross-section on the y-z plane at the first jet ($x = 0.5$ mm) for $N_{jet} = 10$ with $D_{jet} = 0.59$ mm where the micro-channel flow is dominant. For $N_{jet} = 5$ with $D_{jet} = 0.19$ mm, streamlines show stronger jet's momentum interaction on the bottom wall of micro-channel. As a result, the thermal boundary layer on the bottom wall of micro-channel, shown in the enlarged view of the temperature distribution, is thinner for $N_{jet} = 5$ with $D_{jet} = 0.19$ mm than that for $N_{jet} = 10$ with $D_{jet} = 0.59$ mm. This is why the convection heat transfer coefficient for $N_{jet} = 5$ with $D_{jet} = 0.19$ mm is much higher than that for $N_{jet} = 10$ with $D_{jet} = 0.59$ mm.

Fig. 6 represents the wall temperature distributions, averaged over the y-axis of the micro-channel's bottom wall, for different jet diameters and number of jet inlets with $q''_{bot} = 100$ W/cm^2. The temperature distributions are quite uniform

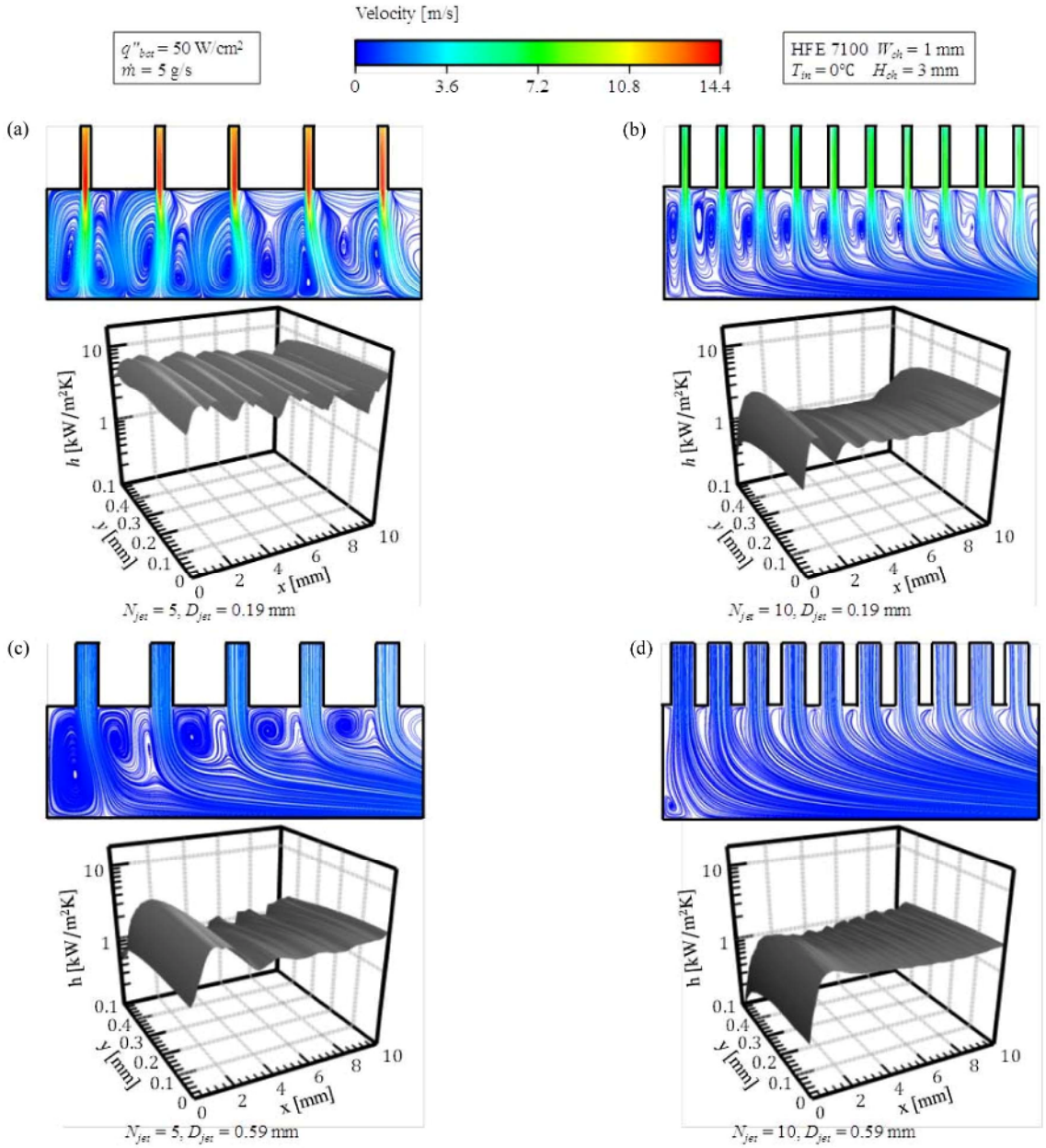

Fig. 4. Streamline plots along the *x-z* plane at y = 0 mm, and convection heat transfer coefficient distributions of the micro-channel's bottom wall at q''_{bot} = 50 W/cm^2 and $\dot{m}$ = 5 g/s for (a) N_{jet} = 5 and D_{jet} = 0.19 mm; (b) N_{jet} = 10 and D_{jet} = 0.19 mm; (c) N_{jet} = 5 and D_{jet} = 0.59 mm; (d) N_{jet} = 10 and D_{jet} = 0.59 mm.

along the x direction for all cases shown in Fig. 6.

Fig. 7 shows variations of mean temperature of the micro-channel's bottom wall for all parametric cases in this study. Note that the cases where the local HFE 7100 temperature reached is higher than its boiling temperature, which is 60.3 °C at 1 bar, are excluded because the phase change is not considered in this study. In Fig. 7(a), at low heat flux, the bottom wall temperatures are maintained at quite low temperatures below 11 °C for all cases, and the effects of jet diameter, mass flow rate and number of jet inlets on the bottom wall temperature are relatively small. At higher heat flux, shown in Figs. 7(b) and (c), the mean temperature of the micro-channel's bottom wall decreases with decreasing jet diameter and increasing mass flow rate due to the increased impingement effects. However, the effects of number of jet inlets on the bottom wall temperature are relatively small compared to the effects of jet diameter and mass flow rate. For both D_{jet} = 0.19 mm and D_{jet} = 0.39 mm, the bottom wall temperature decreases with decreasing the number of jet inlets, while for D_{jet} = 0.59 mm (see Figs. 7(a)-(c)), the bottom wall temperature appears not to be related to the number of jet inlets. This is due to the fact that for large jet diameter, the micro-channel

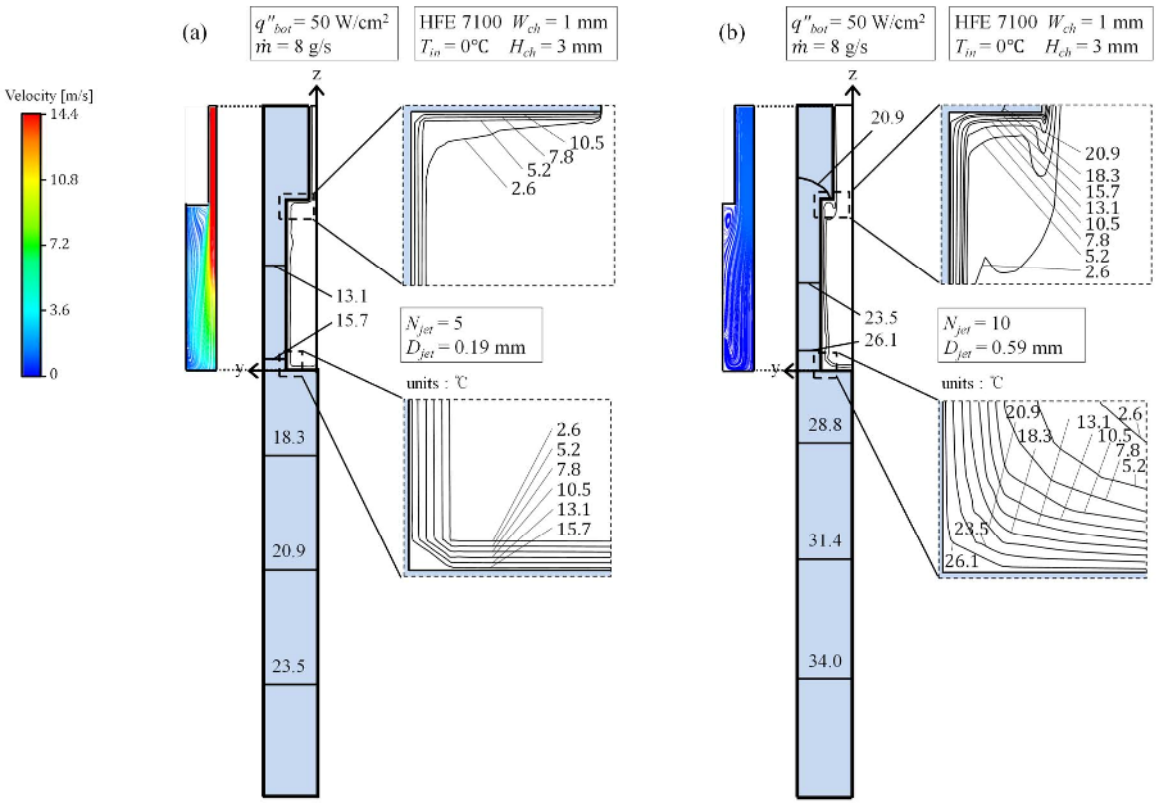

Fig. 5. Streamlines and temperature distributions in the heat sink's cross section at the first jet when q''_{bot} = 50 W/cm² with $\dot{m}$ = 8 g/s for (a) N_{jet} = 5 and D_{jet} = 0.19 mm; (b) N_{jet} = 10 and D_{jet} = 0.59 mm.

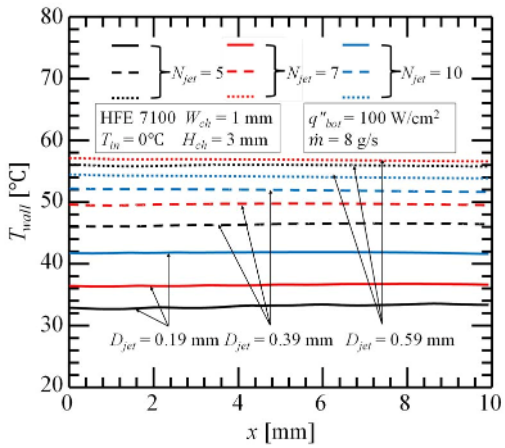

Fig. 6. Temperature distributions of the micro-channel's bottom wall for different diameters of jet inlet and number of jet inlets.

flow is dominant due to the weak impingement effects, thus the effects of number of jet inlets are insignificant. It should be noted that for D_{jet} = 0.19 mm with $\dot{m}$ = 8 g/s (see Fig. 7(d)), the heat dissipation of 150 W/cm² can be achieved using single-phase heat transfer (*i.e.*, without phase change heat transfer) when both the number of jet inlets' values of N_{jet} = 5 and N_{jet} = 7.

Figs. 8(a)-(d) represent the variation of mean convection heat transfer coefficients of micro-channel's bottom wall with different heat flux values of q''_{bot} = 10, 50, 100, 150 W/cm², respectively. The convection heat transfer coefficient generally increases with decreasing jet diameter and increasing mass flow rate due to the increased jet impingement effect. However, for low mass flow rate (*i.e.*, $\dot{m}$ = 2 g/s) with the number of jet inlets of N_{jet} = 10 and N_{jet} = 7, no appreciable changes in the heat transfer coefficient with different jet are shown. The maximum heat transfer coefficient value of 11152 W/m²K can be achieved using N_{jet} = 5 with D_{jet} = 0.19 mm at $\dot{m}$ = 8 g/s, when dissipating 150 W/cm². However, further increase in the heat flux can result in evaporation of HFE 7100, which precludes the use of single-phase hybrid heat sink, requiring the use of two-phase hybrid heat sink instead. For all heat flux values, mean heat transfer coefficient can be achieved above 10000 W/m²K using N_{jet} = 5 with D_{jet} = 0.19 mm at $\dot{m}$ = 8 g/s due to strong jet impingement effect.

4. Conclusions

This study explores the cooling performance associated with single-phase hybrid micro-channel/micro-jet-impingement cooling method. The parametric study on the number of jet inlets, jet diameters, mass flow rate, and bottom wall heat flux is numerically investigated. Key findings are as follows:

(1) With decreasing jet diameter, decreasing number of jet inlets and increasing mass flow rate, heat transfer coefficient of the micro-channel's bottom wall increases since the jet

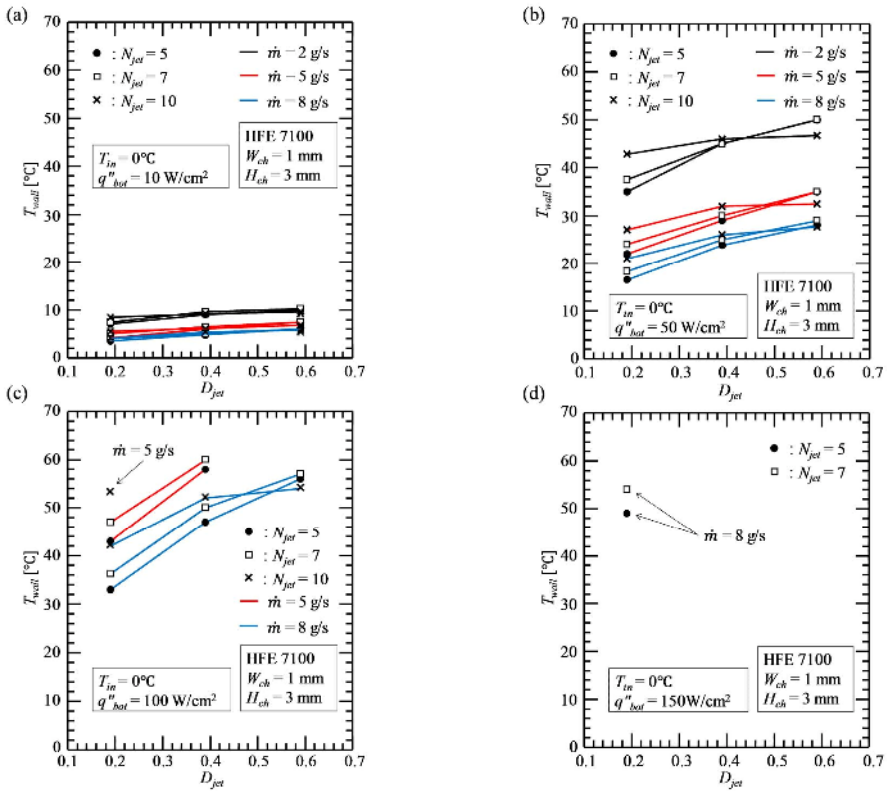

Fig. 7. Variations of mean temperature of the micro-channel's bottom wall with different jet diameters for (a) q''_{bot} = 10 W/cm^2; (b) q''_{bot} = 50 W/cm^2; (c) q''_{bot} = 100 W/cm^2; (d) q''_{bot} = 150 W/cm^2.

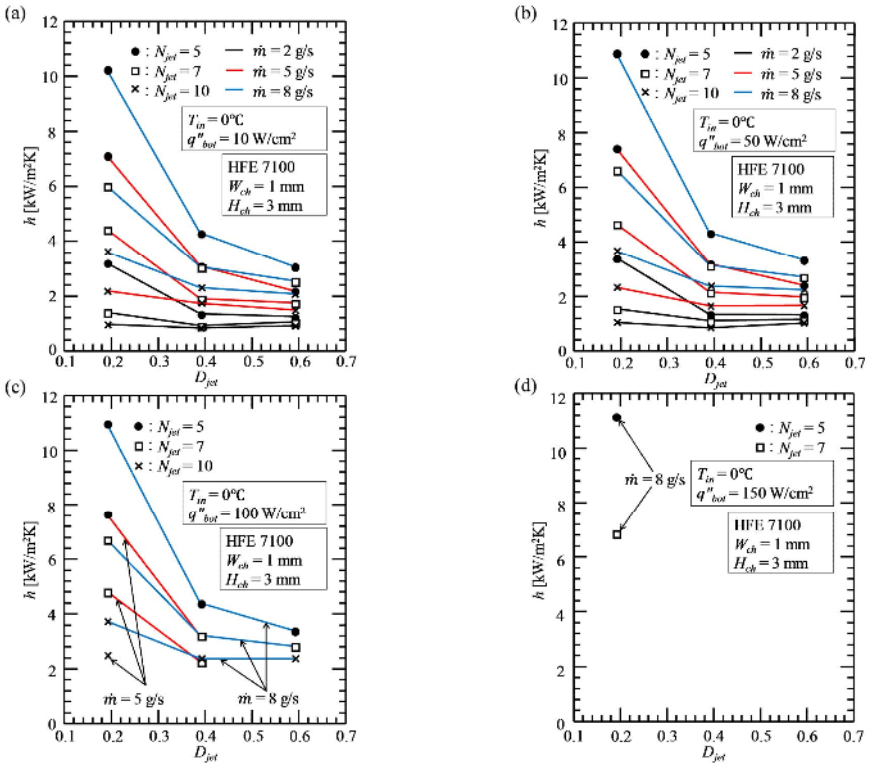

Fig. 8. Variations of mean convection heat transfer coefficient of the micro-channel's bottom wall with jet diameters for (a) q''_{bot} = 10 W/cm^2; (b) q''_{bot} = 50 W/cm^2; (c) q''_{bot} = 100 W/cm^2; (d) q''_{bot} = 150 W/cm^2.

impingement effect is dominant.

(2) The temperature distributions are quite uniform along the micro-channel's bottom wall.

(3) For low heat fluxes, the effects of jet diameters, mass flow rate and number of jet inlets on the micro-channel's bottom wall temperature are not significant, while for higher heat fluxes, the mean temperature of the micro-channel's bottom wall decreases with decreasing jet diameter and increasing mass flow rate. Note that for D_{jet} = 0.59 mm, the largest diameter in this study, the micro-channel's bottom wall temperature appears not to be related to the number of jet inlets since the micro-channel flow is dominant.

(4) The maximum heat transfer coefficient value of 11152 W/m^{2}K can be achieved without phase change by using N_{jet} = 5 with D_{jet} = 0.19 mm at $\dot{m}$ = 8 g/s, when dissipating 150 W/cm^2. For all heat flux values, the mean heat transfer coefficients can be achieved above 10000 W/m^{2}K by using N_{jet} = 5 with D_{jet} = 0.19 mm at $\dot{m}$ = 8 g/s.

Acknowledgments

This work is supported by the Korea Agency for Infrastructure Technology Advancement (KAIA) grant funded by the Ministry of Land, Infrastructure and Transport (Grant 1615009756).

Nomenclature

C_1, C_2 : Empirical constants
c_p : Specific heat at constant pressure
D_{jet} : Diameter of micro-jet
G_k : Production of turbulent energy
H_{ch} : Height of micro-channel
H_{jet} : Height of micro-jet
H_w : Height from unit cell bottom boundary to test surface
h : Convective heat transfer coefficient
k_f : Thermal conductivity of fluid
k_s : Thermal conductivity of solid
k : Turbulent kinetic energy
L : Length of unit cell
L_{jet} : Jet pitch
$\dot{m}$: Total mass flow rate
N_{jet} : Number of micro-jets per one quarter of unit cell
P : Pressure
Pr_t : Turbulent Prandtl number
q''_{bot} : Heat flux applied to the bottom of copper block
Re_{ch} : Channel Reynolds number
Re_{jet} : Jet Reynolds number
S : Modulus of mean rate-of-strain tensor
T : Temperature
T_{in} : Fluid inlet temperature
u_i, u_j : Cartesian components of velocity
u'_i, u'_j : Cartesian components of fluctuating velocity
W : Width of unit cell
W_{ch} : Width of micro-channel
x : Cartesian coordinate
y : Cartesian coordinate
z : Cartesian coordinate

Greek symbols

δ_{ij} : Kronecker delta
ε : Turbulent dissipation rate
μ : Dynamic viscosity
μ_t : Eddy viscosity
ν : Kinematic viscosity
ρ : Density
σ_k : Empirical constant in k transport equation
σ_ε : Empirical constant in ε transport equation

References

[1] A. Naeemi and J. D. Meindl, An upper limit for aggregate I/O interconnect bandwidth of GSI chips constrained by power dissipation, *Proceedings of IEEE International Interconnect Technology Conference* (2004) 157-159.

[2] R. R. Schmidt and B. D. Notohardjono, High-end server low-temperature cooling, *IBM J. Research and Development*, 46 (6) (2002) 739-751.

[3] I. Mudawar, Assessment of high-heat-flux thermal management schemes, *IEEE Trans-CPMT: Compon. Packag. Technol.*, 24 (2) (2001) 122-141.

[4] D. B. Tuckerman and R. F. W. Pease, High-performance heat sinking for VLSI, *IEEE Electron. Dev. Lett.*, 2 (5) (1981) 126-129.

[5] T. M. Harms, M. J. Kazmierczak and F. M. Gerner, Developing convective heat transfer in deep rectangular microchannels, *Int. J. Heat Fluid Flow*, 20 (2) (1999) 149-157.

[6] W. Qu and I. Mudawar, Experimental and numerical study of pressure drop and heat transfer in a single-phase microchannel heat sink, *Int. J. Heat Mass Transfer*, 45 (12) (2002) 2549-2565.

[7] T. H. Park, H. G. Choi, J. Y. Yoo and S. J. Kim, Streamline upwind numerical simulation of two-dimensional confined impinging slot jets, *Int. J. Heat Mass Transfer*, 46 (2) (2003) 251-262.

[8] S. Ashforth-Frost and K. Jambunathan, Numerical prediction of semi-confined jet impingement and comparison with experimental data, *Int. J. Numerical Methods Fluids*, 23 (3) (1996) 295-306.

[9] T. J. Craft, L. J. W. Graham and B. E. Launder, Impinging jet studies for turbulence model assessment—II. An examination of the performance of four turbulence models, *Int. J. Heat Mass Transfer*, 36 (10) (1993) 2685-2697.

[10] M. Angioletti, E. Nino and G. Ruocco, CFD turbulent modelling of jet impingement and its validation by particle image velocimetry and mass transfer measurements, *Int. J. Thermal Sciences*, 44 (4) (2005) 349-356.

[11] D. Cooper, D. C. Jackson, B. E. Launder and G. X. Liao, Impinging jet studies for turbulence model assessment—I.

Flow-field experiments, *Int. J. Heat Mass Transfer*, 36 (10) (1993) 2675-2684.
[12] H. Martin, Heat and mass transfer between impinging gas jets and solid surfaces, *Adv. Heat Transfer*, 13 (1977) 1-60.
[13] D. C. Wadsworth and I. Mudawar, Cooling of a multichip electronic module by means of confined two-dimensional jets of dielectric liquid, *ASME J. Heat Transfer*, 112 (4) (1990) 891-898.
[14] D. J. Womac, F. P. Incropera and S. Ramadhyani, Correlating equations for impingement cooling of small heat sources with multiple circular liquid jets, *ASME J. Heat Transfer*, 116 (1994) 482-486.
[15] Y. Xing, S. Spring and B. Weigand, Experimental and numerical investigation of heat transfer characteristics of inline and staggered arrays of impinging jets, *J. Heat Transfer*, 132 (9) (2010) 092201.
[16] L. M. Jiji, Experimental investigation of single-phase multi-jet impingement cooling of an array of microelectronic heat sources, *Proceedings of the International Symposium on Cooling Technology for Electronic Equipment*, Hemisphere Publishing Corporation, Washington, DC (1988) 333-351.
[17] M. K. Sung and I. Mudawar, Experimental and numerical investigation of single-phase heat transfer using a hybrid jet-impingement/micro-channel cooling scheme, *Int. J. Heat Mass Transfer*, 49 (3-4) (2006) 682-694.
[18] M. K. Sung and I. Mudawar, Single-phase hybrid micro-channel/micro-jet impingement cooling, *Int. J. Heat Mass Transfer*, 51 (17-18) (2008) 4342-4352.
[19] M. K. Sung and I. Mudawar, Effects of jet pattern on single-phase cooling performance of hybrid micro-channel/micro-circular-jet-impingement thermal management scheme, *Int. J. Heat Mass Transfer*, 51 (19-20) (2008) 4614-4627.
[20] T. H. Shih, W. W. Liou, A. Shabbir, Z. Yang and J. Zhu, A new k-ε eddy viscosity model for high reynolds number turbulent flows, *Computers Fluids*, 24 (3) (1995) 227-238.
[21] J. P. Van Doormaal and G. D. Raithby, Enhancements of the simple method for predicting incompressible fluid flow, *Numerical Heat Transfer*, 7 (2) (1984) 147-163.
[22] ANSYS, Inc., *ANSYS Fluent User's Guide*, ANSYS, Inc., Canonsburg, PA (2013).

Seong Hoon Kim received B.S. degree from Sungkyunkwan University, Korea, in 2017. He is currently a M.S. candidate. His research interest includes two-phase heat transfer and its mechanistic modeling.

Hong-Cheol Shin received M.S. degree from Sungkyunkwan University, Korea, in 2018. He is currently a Ph.D. candidate. His research interest includes two-phase heat transfer and its mechanistic modeling.

Sung-Min Kim is an Assistant Professor at Sungkyunkwan University from 2015. He received his Ph.D. degree from Purdue University, USA, in 2012. His research interests include two-phase flow and heat transfer, high-heat-flux and high-efficiency heat transfer system, thermal energy storage, and high-performance fluid machinery.